UNIVERSITAT POLITÈCNICA DE CATALUNYA
BARCELONATECH
Escola d'Enginyeria de Barcelona Est

FINAL DEGREE PROJECT

Degree in Biomedical engineering

CHARACTERIZATION OF CALCIUM PHOSPHATE STRUCTURES OBTAINED BY 3D PRINTING

Author: Antonio Molina Herrero
Director: Maria Pau Ginebra Molins
Supervisor: Santiago Raymond Llorens

Announcement: January 2020

Resum

El processament d´imatges és una eina que s´està utilitzant cada vegada més per extreure, de manera senzilla i ràpida, diferents paràmetres utilitzats per caracteritzar estructures tridimensionals que, mitjançant altres tècniques de caracterització trigaríem molt més temps i serien més costoses.

L'objectiu d'aquest estudi és analitzar els atributs macroscòpics (geometria dels filaments, porositat, superfície específica i concavitat), d'estructures tridimensionals de fosfat de calci amb diferents morfologies dels filaments a partir de les imatges obtingudes per micro-tomografia computeritzada (Micro-CT). A l'estudi es comparen els resultats obtinguts amb tres softwares (CTAN, ImageJ i MeshMixer), així com els obtinguts a partir dels càlculs teòrics a partir de mesures en 2D. També s'han caracteritzat les seccions dels diferents broquets d'impressió utilitzats mitjançant microscòpia electrònica de rastreig (SEM), comparant-los amb la secció dels filaments impresos. Pel que fa a la determinació del grau de concavitat de les diferents estructures, s'ha fet una estimació d'aquest paràmetre tant en 3D, utilitzat una extensió del software ImageJ, com en 2D, a partir de les imatges de les seccions dels filaments (Micro-CT) i dels broquets d'impressió (SEM).

L'estudi ha permès quantificar el grau de desviació existent en els diferents paràmetres morfològics entre els broquets d'impressió i els filaments impresos, malgrat que el fet d'haver utilitzat tècniques d'imatge (SEM i micro-CT) amb diferent resolució també pot haver influït en les diferències observades. Pel que fa a la porositat, els diferents softwares emprats han resultat en valors similars i s'ha observat que quan s'imprimeix estructures amb una mida de porus fix (com és en aquest cas), una mida de filament menor augmenta la porositat del material. Respecte a la superfície específica, el càlcul per malles no ha donat bons resultats, i això pot ser degut a un error a l'hora de reconstruir la malla a partir de les imatges de Micro-CT per l'extensió 3D Viewer de el programa ImageJ. D´altra banda, s´ha pogut observar que, per als càlculs de superfície especifica, no només és important la forma del filament, sinó també la mida de la seva secció; els filaments con una secció petita es repeteixen més al llarg de la peça i per tant el valor total de superfície especifica és més gran que en peces amb una secció més gran. Finalment, en el cas de la concavitat, les dues formes de càlcul (3D i 2D) han donat resultats semblants, i la comparativa en 2D de la secció del broquet d'impressió i la secció del filament ha posat de manifest la desviació existent entre ambdues.

Resumen

El procesamiento de imágenes es una técnica que cada vez se está usando más para extraer, de manera rápida y sencilla, diferentes parámetros utilizados para caracterizar estructuras tridimensionales que, mediante otras técnicas de caracterización convencionales llevarían mucho más tiempo y serían más costosas.

El objetivo de este estudio es analizar los atributos macroscópicos (geometría de los filamentos, porosidad, superficie específica y concavidad), de estructuras tridimensionales de fosfato de calcio con diferentes morfologías de filamentos a partir de las imágenes obtenidas por micro-tomografía computarizada (Micro-CT). En el estudio se comparan los resultados obtenidos con tres softwares (CTAn, ImageJ y MeshMixer), así como los obtenidos a partir de los cálculos teóricos a partir de medidas en 2D. También se han caracterizado las secciones de las diferentes boquillas de impresión utilizadas mediante microscopia electrónica de rastreo (SEM), comparándolos con las secciones de los filamentos impresos. Para poder determinar el grado de concavidad de las diferentes estructuras, se ha hecho una estimación de este parámetro tanto en 3D, utilizando una extensión del software ImageJ, como en 2D, a partir de las imágenes de las secciones de los filamentos (Micro-CT) y de las boquillas de impresión (SEM).

El estudio ha permitido cuantificar el grado de desviación existente en los diferentes parámetros morfológicos entre las boquillas de impresión y los filamentos impresos, a pesar de que el hecho de haber usado técnicas de imagen (SEM y Micro-CT) con diferente resolución también puede haber influido en las diferencias observadas. Para la porosidad, los diferentes softwares usados han dado valores similares y se ha observado que cuando se imprimen estructuras con una medida de poro fija (como es en este caso), una medida de filamento menor aumenta la porosidad del material. Respecto a la superficie específica, el cálculo de mallas no ha dado buenos resultados, y esto se puede deber a un error a la hora de reconstruir la malla a partir de las imágenes de Micro-CT por la extensión 3D Viewer del programa ImageJ. Por otra parte, se ha podido observar que, para los cálculos de superficie específica, no solo es importante la forma del filamento, sino también la medida de su sección; los filamentos con una sección pequeña se repiten más a lo largo de la pieza y por tanto el valor total de superficie específica es más grande que aquellas piezas con secciones más grandes. Finalmente, en el caso de la concavidad, las dos maneras de cálculo (2D y 3D) han dado resultados similares, y la comparación en 2D de la sección de la boquilla de impresión y la sección del filamento han puesto de manifiesto la desviación existente entre ambos.

Abstract

Image processing is a technique that is increasingly being used to extract, quickly and easily, different parameters used to characterize three-dimensional structures that, through other conventional characterization techniques, would take much longer and be more expensive.

The objective of this study is to analyse the macroscopic attributes (filament geometry, porosity, specific surface and concavity), of three-dimensional structures of calcium phosphate with different filament morphologies from the images obtained by computed micro-tomography (Micro- CT). The study compares the results obtained with three software (CTAn, ImageJ and MeshMixer), as well as those obtained from theoretical calculations from 2D measurements. The sections of the different nozzles used by scanning electron microscopy (SEM) have also been characterized, comparing them with the sections of the printed filaments. In order to determine the degree of concavity of the different structures, an estimation of this parameter has been made both in 3D, using an extension of ImageJ software, as in 2D, from the images of the filament sections (Micro-CT) and nozzles (SEM).

The study has allowed quantifying the degree of deviation in the different morphological parameters between the nozzles and the printed filaments, although the fact of having used imaging techniques (SEM and Micro-CT) with different resolution may also have influenced the observed differences. For porosity, the different software used have given similar values and it has been observed that when structures with a fixed pore size are printed (as in this case), a smaller filament measure increases the porosity of the material. Regarding the specific surface, the calculation of meshes has not given good results, and this may be due to an error when reconstructing the mesh from the Micro-CT images by the 3D Viewer extension of the ImageJ program. On the other hand, it has been observed that, for specific surface calculations, not only the shape of the filament is important, but also the measurement of its section; the filaments with a small section are repeated more throughout the piece and therefore the total value of specific surface is larger than those pieces with larger sections. Finally, in the case of concavity, the two ways of calculation (2D and 3D) have given similar results, and the 2D comparison of the section of the nozzle and the section of the filament have revealed the existing deviation between both of them.

Acknowledgements

We have to acknowledge Dr. Antonio Riveiro Rodriguez and Prof. Juan María Pou Saracho from the University of Vigo for collaborating with us in the manufacturing of the laser-cut nozzle discs without which this whole project would not have been possible.

We also acknowledge Emilie Thorel for her work in the development and optimisation of the printing process with every nozzle geometry and for manufacturing the final scaffolds that were analysed in this project.

List of figures

List of tables

Index

1. Introduction

1.1. Porous scaffolds for bone regeneration

Bone is one of the tissues with higher capacity for regeneration. However, this capacity is not unlimited. Like any tissue, when a defect exceeds a critical size, the body is not able to regenerate itself and the use of a bone graft is required. This substitute can have a natural or synthetic origin and will serve as support and guide the action of regenerating by the bone cells. The gold standard is the autograft, however this solution requires a second surgery in order to obtain the bone [1]. Moreover, the source is very limited. Other natural origin grafts like allografts and xenografts appear as an alternative. However, this solution leads to highly processed materials with considerably reduced biological properties when compared to the autografts. Finally, synthetic bone grafts represent a promising choice as its nature allows to tune its physicochemical and biological features optimizing them to present not only osteoconductive properties but also osteoinductive and angiogenic ones. Among the synthetic bone grafts, calcium phosphate (CaPs) based ones have been widely studied. However, they not promote osteogenesis sufficiently. Finally, the use of synthetic bone substitute with endowing intrinsic osteoinductive properties is one of the most promising bone substitute graft.

Some studies indicate the porosity in the scaffolds as one of the key factors for the bone regeneration. The key parameters in the porosity are the interconnectivity of the pore network, the pore size and the pore shape. An interconnected pore network allows the vascularization of all the area and later tissue colonisation. Many studies have been carried out searching for the optimal pore size in a scaffold [1], however the conclusions are not clear and some studies contradict others; What is clear is that the pores have to be big enough to allow the vascularization (50 µm), but if they are larger than a certain size (500 µm) the scaffold is not acting anymore as a scaffold [2]. Finally, the pore shape is the less studied of the parameters but recent studies suggest that this parameter may be crucial for the scaffold biological features. Barba et al. reported that a concave porosity resulted in a higher presence of osteoclast-like cells in the histological assessment; also, these structures produced the accelerated bone formation when compared to conventional calcium phosphate with the same architecture [3]. So, spherical concave macroporosity have a higher osteinduction potential [4].

Many different techniques have been developed for the conformation of CaP porous structures: Granulation [5], foaming [6], leaching [7] and freeze drying [8] are the most popular traditional techniques. With the development of the digital technologies and democratization of computers, additive manufacturing techniques have emerged as a very promising alternative. Direct ink writing (DIW) of ceramic slurries mixed in a gel phase (a.k.a. Robocasting) [8] has recently become very popular for the manufacturing of CaP scaffolds. This technique allows a precise control of the internal porosity

of the structures ensuring a high reproducibility and allowing to obtain an interconnected pore network. In addition, DIW, enables to define the external shape of the scaffold allowing to produce patient specific parts. However, conventional DIW processes result in convex surfaces, since the scaffold strands are obtained by extruding a paste through a circular nozzle, which leads to a cylindrical shape. However, as shown by Lewis et al., non-cylindrical filaments can be extruded by modifying the shape of the nozzles. This offers a strategy to tune the degree of concavity of the inner scaffold surface [9].

1.2. Development of calcium phosphate scaffolds with non-cylindrical strands by DIW

Scaffolds with non-cylindrical strands were produced by the company Mimetis Biomaterials by modifying the traditional DIW system reported elsewhere[4] with a customized modular extrusion nozzle. The design was conceived to fit different discs in its bottom extremity as represented in Figure 1. Discs with 3mm in diameter and a central perforation with various geometries were produced. This nozzle setup was assembled to a ceramic ink cartridge and assembled in a direct ink writing device.

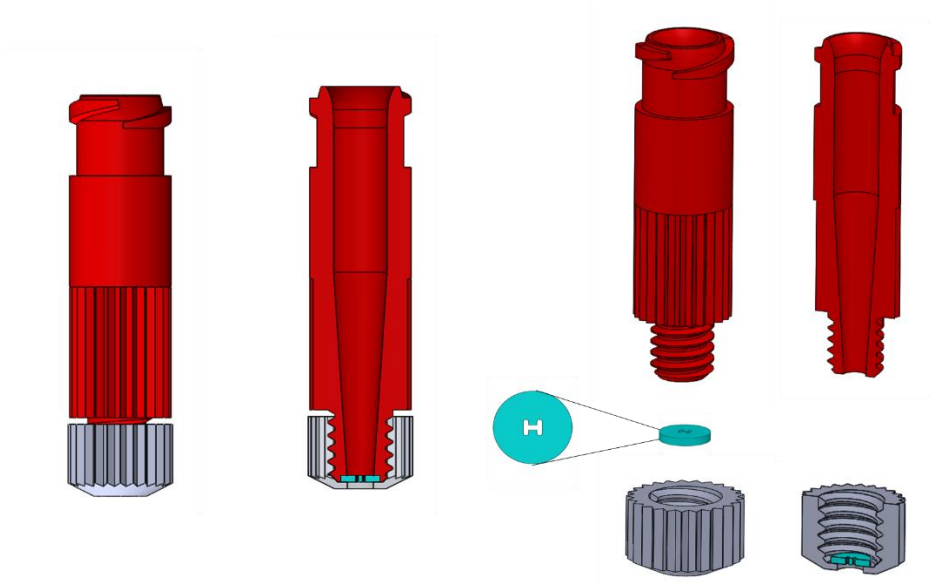

Figure 1. Schema of the custom modular nozzle design. Red: Upper part of the nozzle with ¨Luer lock¨ standard connector on the top section. Grey: Lower part of the nozzle. Unscrewable to fit the custom disk. Turquoise: Disc with variety of central orifice design.

The scaffolds were printed in *Mimetis* with a fixed pore size (250 µm) in the XY plane in order to make the scaffolds similar enough to be able to compare results between them. Five different geometries were studied and compared to each other and with a control group with cylindrical scaffold strands.

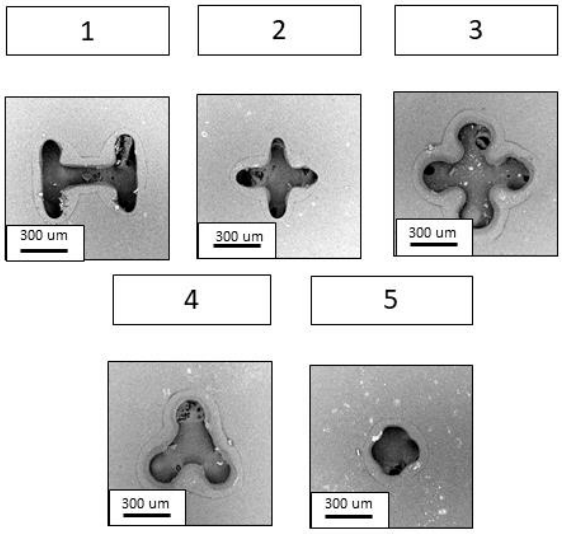

Figure 2. SEM image of the different disc central orifices

1.3. Image processing state of the art

The image processing is one of the most used techniques due to their low cost; also, thanks to the increasingly powerful technology, these processes are becoming more accurate and faster [10]. One of the early studies in use SEM images for characterization was made by Zeman and Denault [11]. Zeman et al. investigate the effect of contrast, resolution and grayscale level in the detection of smaller pores; with a conclusion that the higher resolution images usually led to detection of smaller pores [11]. Nowadays, the more common approaches are based on the use of Micro-CT, because it allows the reproduction of the 3D scaffolds, something that cannot be done with the other technique [12]; however, the Micro-CT images have less resolution than the SEM images, and this affect in the calculous of 2D parameters (area, perimeter, thickness). So, in the majority of studies its used the 2 method: the calculous of 3D parameters with Micro-CT images and the calculous of 2D parameters with the SEM images [13].

Image processing also depends on the image contrast to do the segmentation. The majority of image software only works with binary images (images with their pixel value is 0 or 1), and the majority of Micro-CT and SEM images are grayscale images (images with their pixel value is between 0 and 255). To transform a grayscale image into a binary image there is a need to do a threshold [14]. This process set a value between 0 and 255, if a pixel has a lower value than the threshold, the value of these pixel will become 0, otherwise it will become 1, transforming the grayscale image into a binary image. So, images with low contrast have very grouped pixel values, so segmentation will be more difficult and this will affect future calculations [15].

1.4. Objectives of the study

One of the main problems of using porous scaffolds for in vivo testing is to characterize in detail all the geometric parameters in order to better understand how these characteristics affect bone formation. A small change in the concavity or porosity of the scaffold can affect bone regeneration positively or negatively; so, there is a need to use powerful tools to analyse these parameters, such as image processing techniques.

The complex and imbricated shape of these 3D structures can be studied by advanced imaging techniques such as micro computed tomography (Micro-CT) and scanning electron microscopy (SEM). The image processing to extract quantitative information of these images is at the same time promising and challenging. These tools are increasingly used due to its immediacy and reliability. With them, morphological properties of three dimensional structures can be studied and provide morphological and structural information of a big interest for the design and characterization of new scaffolding shapes for tissue engineering [13], [14]. Normally more than one program is used in these analyses, either to perform segmentation processes or compare results between them. De Souza et al. use ImageJ to do the pre-processing of the images and the CTAn to calculated the macro porosity [16].

In this context, the general objective of this study is the analysis of the geometrical properties of 3D-printed scaffolds with different strand shape. Moreover, two specific objectives are targeted:

a) The comparison of various geometrical parameters obtained using different image processing methods.
b) The comparison between direct 3D imaging techniques and the results obtained by theoretical calculations from 2D images of the nozzle morphology.

2. Methods

2.1. Data acquisition

2.1.1. Scanning Electron Microscopy of the nozzles

Sample preparation

The nozzle discs were coated with a thin carbon layer by carbon vaporization (10 pluses) in order to avoid electrostatic charges during the SEM imaging process.

Settings

All data were acquired with a desktop SEM (Zeiss Neon40 EsBCrossBeam, Zeiss, Oberkechen, Germany) using a beam intensity of 10kV, a field of view of 1.07 mm, a magnification of 250x and a Backscatter electron detector (BSD). This detector is used because it provides a data with a better contrast that later permits an easier segmentation.

2.1.2. Micro Computed Tomography of the 3D-printed scaffolds

A micro computerized tomography (SkyScan 1172, Bruker Micro-CT, Kontich, Belgium) was used to collect stacked topographies of the different scaffolds.

Sample preparation

All the samples were analysed individually in a holder with disc. These disc where attached to the holder with dental wax.

Settings

Data were collected in 0.2^{o} rotation steps between 0 and 180^{o} with an exposure time of 3100 ms. The machine was operated with a source voltage of 100kV and source current of 100 µA. The image pixel size was 26,31 µm.

Image reconstruction

Reconstructions were carried out in order to transform the data acquired in polar axis to a cartesian system. The software package NRecon (Bruker Micro-CT, Kontich, Belgium) was used for this purpose. Images were recorded as stacks in BMP format. Beam-hardening correction and alignment optimization were applied to the reconstructions. Reconstructions were realigned according to the original printing planes using Data Viewer (SKYCAN´s Data Viewer, Bruker Micro-CT, Kontich, Belgium).

2.2. Image standardization and preconditioning

Before its characterization, images were standardized and binalized in order to have a comparable data. This procedure consisted in:

2.2.1. Scanning Electron Microscopy (SEM)

2.2.1.1. Standardisation

In this case, no particular standardization procedure was required as the studied subject is the disc used for extruding the strands and not the 3D structure, no region or volume of interest has to be established. Only by centring the disc central orifice geometry in all the images at the same magnification of 250x and resolution of 1.05 um/px, the acquired images can be considered as standardised.

2.2.1.2. Preconditioning

Segmentation

In this case, the traditional grayscale threshold segmentation did not work with sufficient accuracy as both regions had overlapping grey values in the histogram. As an alternative to traditional greyscale threshold segmentation, a machine learning segmentation solution was used (Ilastik, [17]). Ilastik is a software where the user labels the different regions observed in the image and, by using a family of algorithms called *tracking-by-assignment* [18], the program tries to separate the two regions in the whole image.

The program provided a Pixel Classification workflow to create a segmentation of multidimensional image data. This workflow allowed to classify some examples for each pixel by painting brushstrokes in the data. After that, the tracking method in Ilastik ([17]) found the probable linking of all detections through a global optimization. The prediction was refined after by drawing additional annotation strokes [18].

After exporting the segmented images from Ilastik, images were post-processed with Fiji (Fiji, ImageJ,[19]) in order to remove noise and artefacts. It was used a *remove outliers* filter in order to eliminate all the white pixels outside the section and a close and open operations to eliminate black pixels inside the figure without changing the initial structure [20]. The results can be seen in the Figure 3; despite observing some errors (black pixels) in the final image, the segmentation is good enough to work with it.

Figure 3. Pattern 1 image segmentation process: A) Original raw image, B) Image segmented with Ilastik and C)Image after Fiji noise reduction. 300µm scalebar.

2.2.2. Micro-CT

2.2.2.1. Standardization

- Homogenize the resolution

In this case all the data were acquired with a same resolution of 26.300073 µm/px. Otherwise, all the images should have been reduced in resolution to the minimum resolution found in the dataset in order to obtain a homogenized resolution and be able compare images. This procedure can be achieved by using the tool Image > Scale in Fiji (Fiji, ImageJ,[19]). This process can be done in this way in this work because the voxels isotropic (every voxel have the same length on each side). If this were not the case, it would have to find a way to homogenize the resolution by also homogenizing the stacks/µm.

- Define a volume of interest (VOI)

A square cuboid with a length and width of 5.42 mm and a height of 4.367 mm (corresponding to 206 px square images and 167 images in the Z stack) was chosen as standard VOI. This VOI was obtained by cropping all image stacks of the different sample conditions with an image analysis software (CTAn, Bruker Micro-CT, Kontich, Belgium). First ROI tool was used to define a center square of 5.42 mm (206 px) height and width. Then, ROI was imported in the 167 images to create the VOI. The initial and final volumetric reconstruction could be seen in the Figure 4.

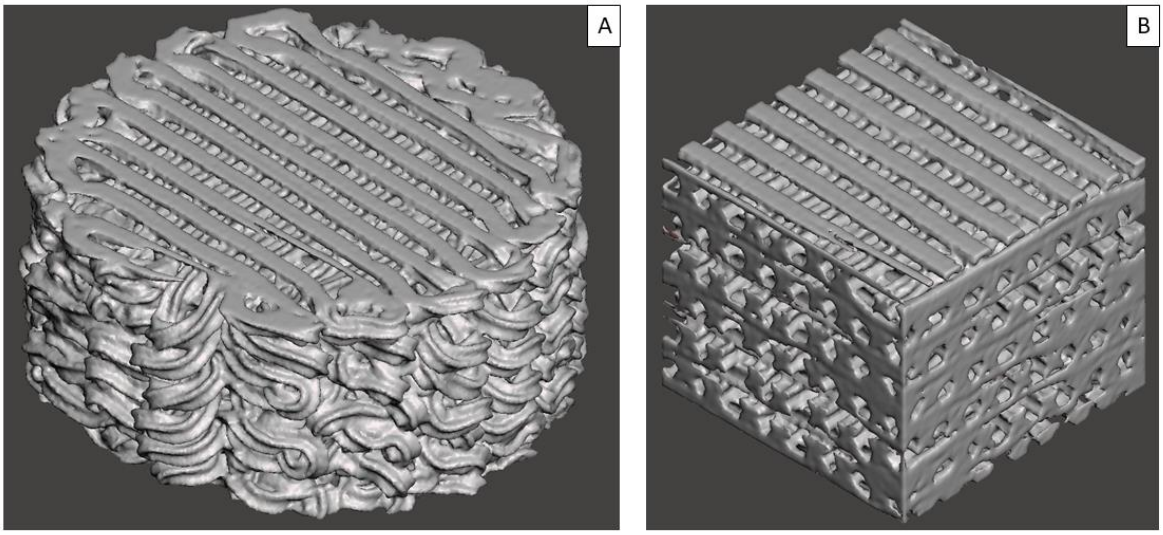

Figure 4. Pattern 2 before (A) and after (B) applying the VOI cropping.

2.2.2.2. Preconditioning

Segmentation

The spectral resolution of the imagers was reduced from the initial 8 bits quantization (grayscale image with pixel dynamic range from 0 to 255) to a 2 bits quantization (binary image with pixel dynamic range from 0 to 1)[21]. This reduction was carried out with an image analysis software Fiji (Fiji, ImageJ,[19]). The "thresholding" tool can be found inside the menu "image > adjust". Within this tool, a threshold is defined and all the pixels in the stack above this value are labelled as material (in white, pixel =1) and all the pixels below this threshold are labelled as void (in black, pixel=0). The definition of this threshold is usually a critical step in the image analysis process and multiple methods have been studied and reported [22] to fairly define this value (e.g. Otsu's method). However, in our case, the radio opacity of both phases can be clearly distinguished in the histogram (Figure 5.A) where we observe a bimodal distribution with non-overlapping peaks. For this reason, this threshold value is not critical in our segmentation process and we can define any value within the central plateau of the histogram. As all the samples have been analysed with the same conditions and in addition the sample material is the same in all the cases, it is fair to define a same threshold value for all the conditions. We have chosen the value 72 as threshold.

We defined a threshold of 72 (can be any value, 72 is the value that it is going to be used in this project) for all the data. With this procedure is obtained two labelled regions corresponding to material and void. The results can be seen in the Figure 5.

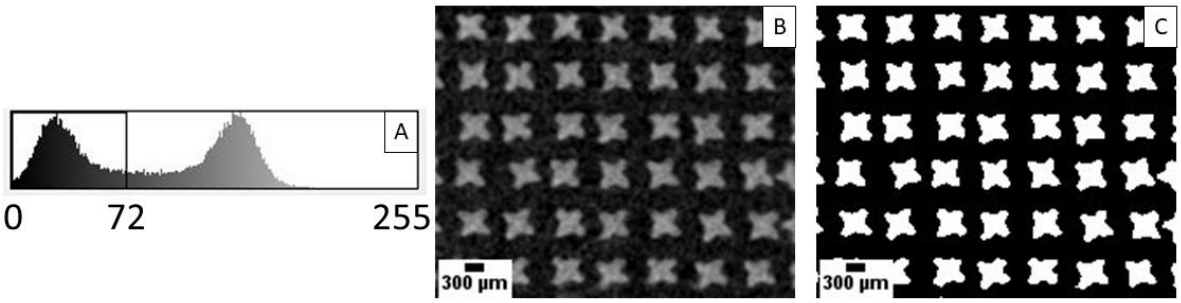

Figure 5. Histogram (A), slice image before segmentation (B) and slice image after segmentation for the sample condition "Pattern 2" (C).

Noise reduction

After the binarisation process, image artefacts can be eliminated with a noise reduction filter. However, it is not advisable to do so because image analysis software usually use a median filter to reduce noise. A median filter picks the N x N neighbour pixel values and calculates the median value as depicted in Table 1 with an example where N=3.

Table 1.Median filter N=3. Centre pixel value before filter (left) and centre pixel value after filter (right) [16]

1	0	1
0	0	1
1	0	1

1	0	1
0	**1**	1
1	0	1

These median filters can eliminate information (like closed porosity) and this can modify the results.

No noise reduction technique was used in the Micro-CT because like it said before, the median filters can modify the results .However, if any noise reduction technique is used; instead of this filter, a noise reduction is achieved by using the tool Process > Noise > Despeckle in Fiji (Fiji, ImageJ,[19]). A despeckle filter is the same as median filter, this filter can be applied multiple times and in a stack of images, in the Figure 6 it can see the difference before applied a despeckle and after. As a results, the image is smoother; but, information that will change the final results has been lost in the process.

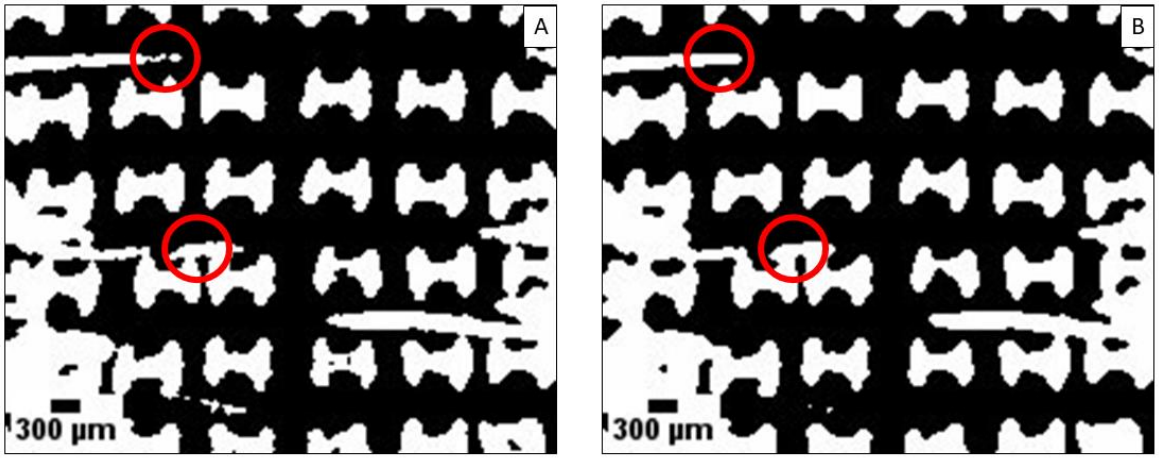

Figure 6. Pattern 1 image before (A) and after (B) applying a despeckle filter. The red circles highlight the main changes.

Meshing

Some of the image analysis carried out in this study were based on 3D meshes of the scaffold. For this reason, the segmented image stacks had to be previously transformed to a three-dimensional meshes of triangles know as Standard Tessellation Language (STL) format. The procedure carried out consisted in the following steps: First, with Fiji (Fiji, ImageJ,[19]), after the binarize, a plugin called 3D viewer[23] was used. After that, a menu popped up and the option "display as a surface" was selected (the predetermined option is "display as volume"). Finally, a 3D view appeared and the result could be saved in STL format, like depicted in the Figure 7.

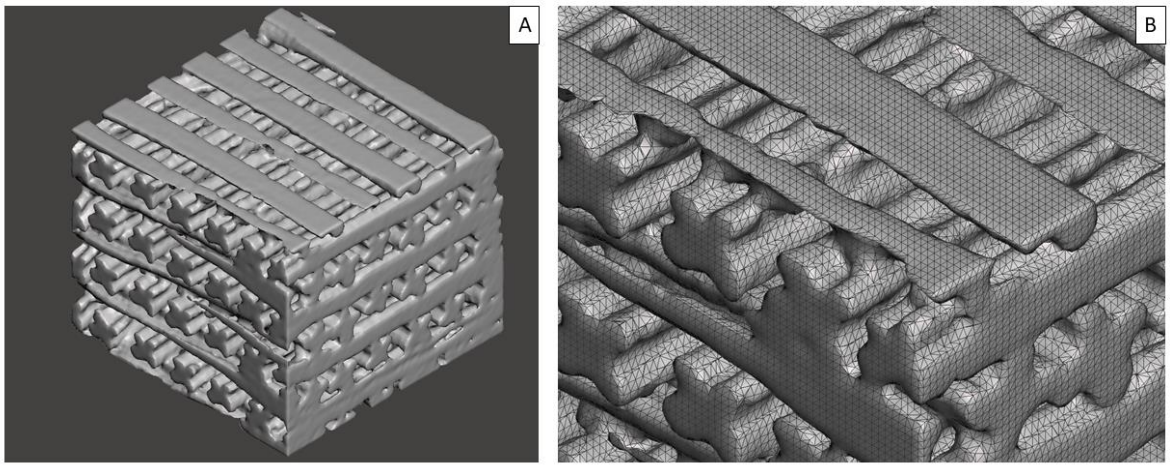

Figure 7. (A) STL mesh of the Pattern 3 and (B) its wireflame.

2.3. Quantification of image attributes

2.3.1. Strand cross section geometrical parameters

The area and perimeter attributes were calculated using the selection tool in Fiji from the cross section view. First, there is a need to do a crop in order to get only one strand for each calculation.

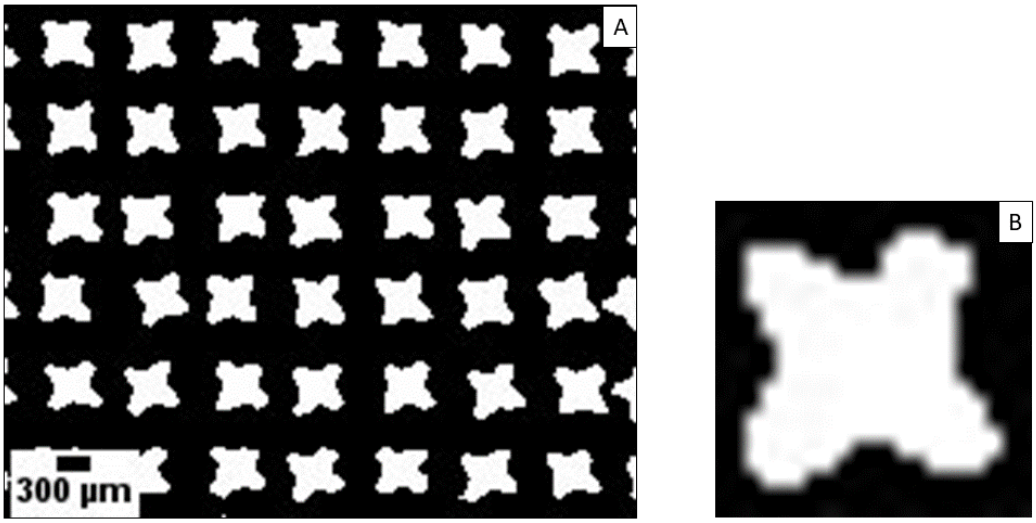

Figure 8. A) Pattern 2. B) Crop of one filament section

The *selection* tool creates a selection that encompasses all except the strand section, so with the tool *make inverse* its create a selection that only encompasses the filament section. Finally, with the tool *measure* the perimeter and area results are calculated.

This attributes are calculated with the nozzle disc (SEM) and the scaffold strand (Micro-CT) in order to compare these two parameters between them. The Micro-CT calculations were made with 5 different strands per condition and the value used for subsequent calculations in other sections corresponded to the average value for each condition. For the SEM images it was only done with a sample due to the limited availability of the discs.

2.3.2. Porosity percentage

We define the porosity of the material as the fraction of the void spaces volume in a material over the total volume.

There are two types or porosity: open porosity and closed porosity. Open porosity is defined as the fraction of the total volume where the pores are joined together and connect with the outside of the material. Meanwhile, closed porosity refers to the fraction of the void spaces in a material that do not connect with the outside.

Due to the resolution and accuracy of the techniques used in this work, in all the cases the measured porosity will correspond to pores larger than 1 µm. What in other works is referred to as macro-porosity [4].

2.3.2.1. Calculation from the 3D micro-CT image using different software's

This porosity percentage will be calculated using three software's:

ImageJ (Fiji, BoneJ)

To calculate the porosity percentage, the Fiji (Fiji, ImageJ,[19]) plugin BoneJ [24] is used. This plugin calculates the porosity by counting the number of black voxels over the number total of voxels in the binarised image stack.

CTAn

CTAn uses the tool "Custom processing > 3D analysis" in order to calculate the porosity percentage. The tool "3D analysis" calculates porosity in the same way as Fiji does, by counting the number of black voxels over the number total of voxels [25].

MeshMixer

With the plugin 3D viewer, a Micro-CT sequence of images can be rebuilt in order to use mesh software like MeshMixer. With this software, the volume of the object can be measure in the tool *stability,* after that, with the use of the Equation 1 the porosity can be calculated.

$$Porosity = \left(1 - \left(\frac{Vol_{mesh}}{Vol_{VOI}}\right)\right) * 100 \qquad \text{Equation 1}$$

2.3.2.2. Theoretical calculation using the 2D section of the filaments

Another approach can be made to calculate the porosity by calculating the area of the filaments that make up the scaffold and extrapolating it to 3D with Equation 2. The area of the filament was calculated in Fiji.

$$Porosity = \left(1 - \frac{Area_{strand} * Number_{strands} * ROI_{length}}{Volume_{VOI}}\right) * 100\ [\%] \qquad \text{Equation 2}$$

The scaffold is composed by strands, so the area of every strand (A_{strand}) multiplied by the length of the strand (ROI_{length}) and the total number of strands in the VOI ($Number_{strands}$) will give the material volume in the VOI; After that, the division of this value over the VOI volume ($Volume_{VOI}$) will give the

material percentage. Finally, if we subtract this value to 1, the result will be the porosity percentage of the scaffold.

Obs.: In this approximation we assume that all the strands are completely linear, and perfectly aligned to the VOI directions. We also assume that all of them have the same length equal to the VOI width or length.

2.3.3. Pore size distribution

This value represents the percentile size distribution of the porosity. The results were obtained from the tool "Custom Processing > 3D analysis > trabecular thickness" of CTAn [26].

The trabecular thickness routine calculates these values by using two image process: Skeletonisation and Sphere fitting.

Skeletonisation is a process for reducing foreground regions to a skeletal structure that preserver the extent and connectivity of the original region[27]. The process is made by applying repeatedly erosions until the figure is as skeletal as possible without losing its shape.

In the Figure 9 there is an example about the final results of a skeletonisation.

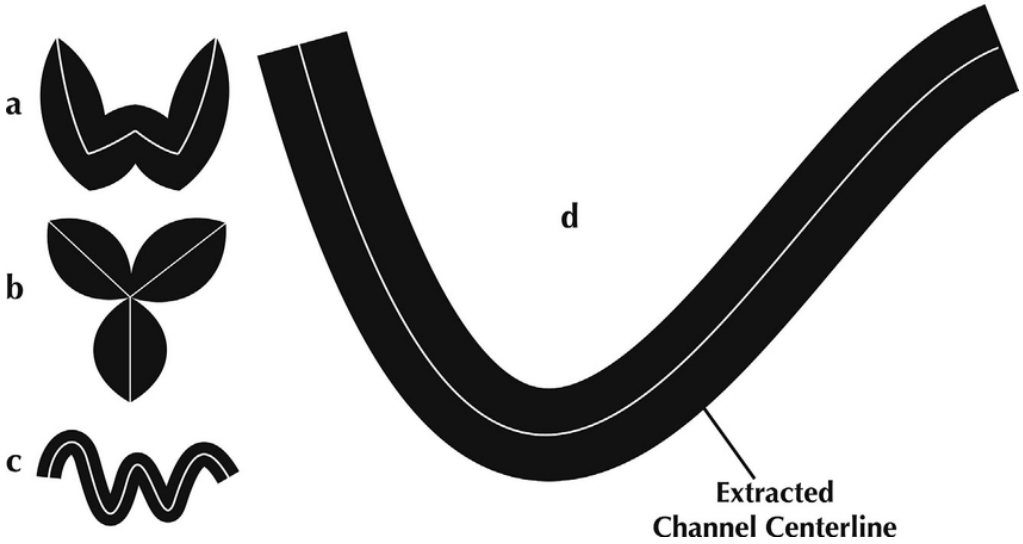

Figure 9. Schema of a skeletonisation process [28].

On the other hand, a sphere fitting is a process that create spheres to measure with two conditions:

- The spheres need to contain a part of the skeletonisation but there is no need to be centred in the skeletal.
- The sphere has to be as big as possible, but, it cannot exceed the initial material size.

With these two conditions the program creates spheres that are used to measure spaces. The constraints are that the sphere can only grow within the regions where the pixels equal to 1, in others words, with the material pixels.

To apply these measurements to the void regions and be able to calculate the pore size distribution, there is a need to make an inverse threshold (make the pixel with value bellow 72 equal to 1 and 0 the others). With this change, CTAn will detect the void as material and study the void regions.

2.3.4. Specific surface area (SSA)

In this work, the SSA will be defined as the division between the surface of the material per unit of volume of material [$\mu m^2/\mu m^3$]. This way, the measurements stay independent from additional physical parameters that cannot be determined by image analysis (*i.e.* material density to obtain mm^2/g).

2.3.4.1. Calculation from the 3D micro-CT image using different software

ImageJ (Fiji,3D Shape)

Fiji image analysis software incorporates a plugin named "3D Shape"[29] that allows us to calculate the SSA from an image stack. This plugin calculates the surface of a scaffold by estimating the fractal dimension on topographic surfaces [29], based in the Mapfractalcount plugin . After the surface is calculated is divided by the volume of the material previously calculated with the plugin BoneJ (see section Porosity percentage).

CTAn

CTAn software calculate the surface in the same way as the pore size distributions, by using first and skeletonisation and after that a sphere fitting. The difference with the pore size distribution is the threshold (the values bellow 72 equal to 0 and 1 the others). After that, this value will be divided by the volume of the material calculate before in the porosity section (see section Porosity percentage).

MeshMixer

With mesh analysis software (MeshMixer, Autodesk) the surface of the material could be calculated by using the tool *stability*. Afterwards, with the Equation 3, the specific surface area could be calculated.

$$SSA = \frac{Mesh_{surface}}{Vol_{VOI}} \qquad \text{Equation 3}$$

2.3.4.2. Theoretical calculation using the 2D section of the filaments

Similar to how it was done in the porosity section, it can also calculate the specific surface area by calculating the area of the filaments that make up the scaffold and extrapolating it to 3D with Equation 4. The perimeter of the strand has to be previously calculated by Fiji.

$$Specific\ Surface\ Area = \frac{Perimeter_{Strands} * Number_{strands} * ROI\_length}{Volume_{VOI}} \qquad \text{Equation 4}$$

We can approximate the surface area of the material inside the VOI by multiplying the perimeter of every strand (Perimeter $_{Strands}$) by the length of the ROI (ROI $_{length}$) and by the number of strands in the VOI (Number $_{Strands}$). Then, by dividing this value over the VOI volume (Volume $_{VOI}$) we can obtain the specific surface area of the sample.

2.3.5. Concavity

There are many different and valuable definitions of concavity in the literature. For this project, we will adopt the traditional nomenclatures and definition used for lens: A shape is convex when any two points that are inside the shape, the line between these two is also inside the shape; otherwise the shape is concave [30]. This comparison can be seen in the Figure 10.

Figure 10. Concavity and convexity difference [30].

In order to quantify the level of concavity/convexity in the different structures, different approaches have been used:

*Unlike in the previous sections, this approaches lead to different indexes that illustrate concavity/convexity but are not comparable because each one quantifies a different attribute with different units.

All the approaches are based in the concept of Convex Hull. We define a convex hull as the smallest convex set that contains the figure.

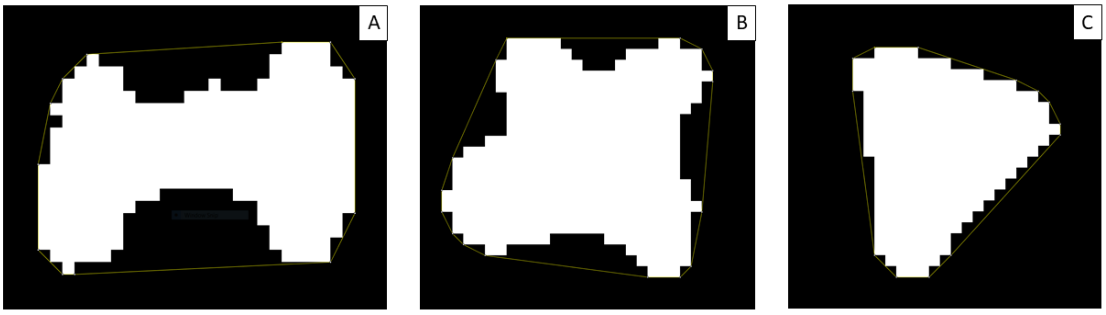

Figure 11. A) Convex hull of Pattern 1. B) Convex hull of Pattern 2. C) Convex hull of Pattern 4.

2.3.5.1. Cross section indexes

In this section, the measurements of convexity are carried out on 2D cross sections of the geometry. For this purpose, two indexes have been defined. Both indexes are based in comparing the attributes of the geometry with the attributes of the convex hull of the geometry.

Measurements were carried out on both, µ-CT images of the strands cross sections (which are more trustworthy but present a lower resolution) and SEM images of the discs' geometries (which are less trustworthy but present a higher resolution). Additionally, the SEM were made for all discs' geometries but not for the nozzles.

A) Perimeter concavity ratio: This index is based on comparing the perimeter of the geometry with the perimeter of the convex hull of the geometry following the Equation 5.

$$Perimeter\ concavity\ ratio = \frac{Perimeter_{strand}}{Perimeter_{ConvexHull}} \qquad \text{Equation 5}$$

As we can intuitively determine observing Figure 12. Schema of the geometry perimeter and the convex hull perimeter in two geometries with different level of concavity., this index will tend to 1 when the geometry approaches to a completely convex shape (i.e. circle) because the shape of the concave hull will be exactly the same as the shape of the geometry and its

perimeters as well. On the other hand, this index will grow (tending to infinite) with structures of higher concavities because the perimeter of the shape will grow with more imbricated structures with concavities (and local concavities and convexities within a concavity) whilst the value of the convex hull will remain stable and more linked to the geometry envelope.

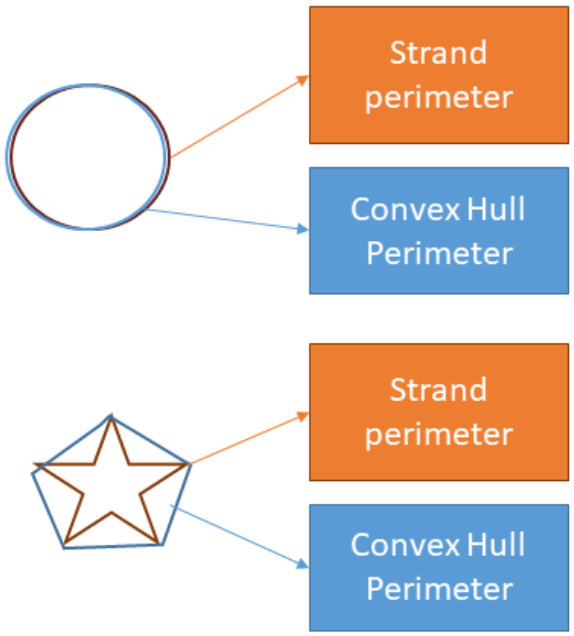

Figure 12. Schema of the geometry perimeter and the convex hull perimeter in two geometries with different level of concavity.

The measurements were carried out in Image J by first selecting the perimeter of the binarised image of the cross-section (*create selection-make inverse*) and calculating its perimeter (*analyse-measure)* and then creating a convex hull selection *(selection-convex hull)* and also measuring the perimeter of this selection *(analyse-measure).* Then these two perimeter values were listed in a calculation table (*Excel*) and the concavity index was calculated for each sample. A total of 5 samples were used in the uCT calculations whilst only one measurement was possible in the SEM data.

B) Surface concavity percentage: This index is based on measuring the percentage of area of the convex hull that correspond to concavities. The following formula has been defined for this purpose:

$$Surface\ Concavity\ percentage = \frac{Area_{ConvexHull} - Area_{Strand}}{Area_{ConvexHull}} * 100\ [\%]$$ Equation 6

As we can observe in Figure 13. Schema of the concave area in two geometries with different concavities., the more concave the structure is, the more the convex hull will differ from the geometry shape and more convex area will appear inside the concave hull (understanding convex area as the region inside the convex hull that does not correspond to a region within the geometry).

In the case of a completely convex structure (i.e. circle), the concave hull perfectly corresponds to the geometry shape and the convex area is inexistent, then, the surface concavity percentage is 0. However, the more the geometry presents concavities, the more the convex hull differs from the geometry and the higher the surface concavity percentage is (tending to 100%).

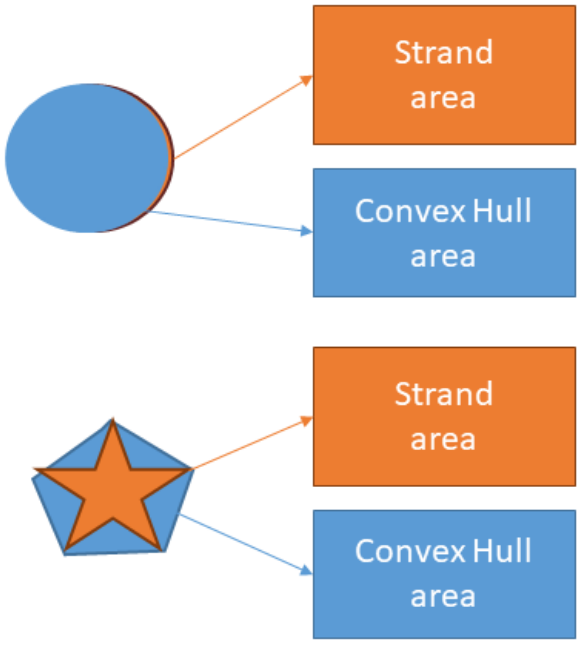

Figure 13. Schema of the concave area in two geometries with different concavities.

The measurements were carried out in Image J by first selecting the perimeter of the binarised image of the cross section (*create selection-make inverse*) and calculating its internal area (*analyse-measure*) and then creating a convex hull selection (*selection-convex hull*) and also measuring the area inside of this selection (*analyse-measure*). Then these two areas were listed in a calculation table (*Excel*) and the surface concavity percentage was calculated for

each sample. A total of 5 samples were used in the uCT calculations whilst only one measurement was possible in the SEM data.

2.3.5.2. Volumetric convexity assessment

This method is based in a plugin developed for the image analysis software Fiji (Image J [19]) named Quickhull Algorithm [30]. This algorithm calculates the convexity y of a 3D structure by estimate the fractal dimension on topographic surfaces [29], based in the Mapfractalcount plugin. After estimated the surface, the program constructs a convex hull and calculate the similarity between the convex hull and the surface. The convex hull is the smallest convex set that contains the figure, the more similar the figure is to the convex hull, the more convex it is.

2.4. Statistical analysis

The results are presented as mean values ± standard error. Minitab Software [31] was used for statistical analysis Statistical comparisons between strands cross section results were performed using ANOVA test followed by Tukey`s post hoc test. Statistical significance was defined as $p < 0.05$.

3. Results and Discussion

Five patterns were analyzed, together with the control which was obtained using a circular nozzle. The patterns are coded as Control, 1, 2, 3, 4 and 5.

3.1. Scaffold's overview

In Figure 14 the SEM images of the nozzles are shown, together with the filament sections in the sagittal view of the printed scaffolds visualized by Micro-CT.

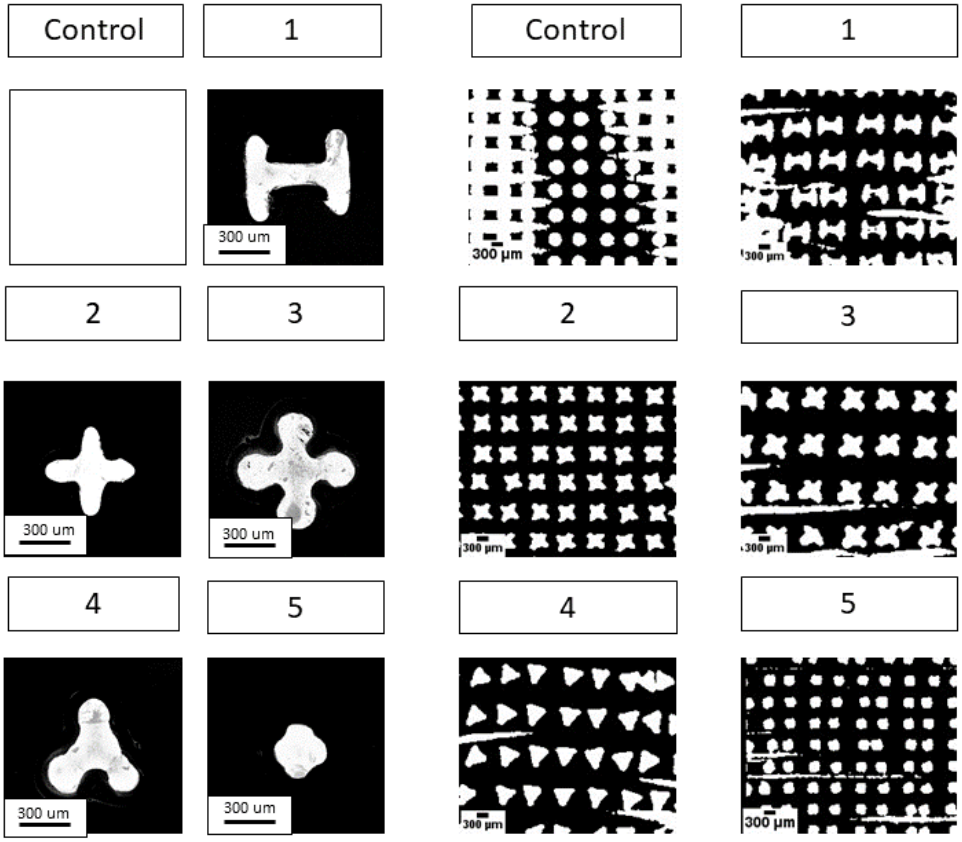

Figure 14.Left: Image of the nozzles by SEM; Right: Scaffold's sagittal view by Micro-CT.

It can be seen that the strands geometries are pretty similar between the SEM and the Micro-CT images; however, there are differences in the pattern 4 (in the SEM image it has a concavity in the base while in the Micro-CT image it is not found). This difference may be due to in the printing process that concavity disappeared.

3.2. Nozzle and strand cross section geometrical parameters

The results of the area values are summarizes in the Table 2 and in the Figure 15.

Table 2. Area values

	Strand cross section (Micro-CT) , um^2	**Nozzle orifice (SEM), um^2**
Control	108862± 3301	133965
1	104974± 3673	155794
2	60263± 3462	103356
3	111778± 4171	194934
4	69659± 2002	142874
5	34019± 945	63267

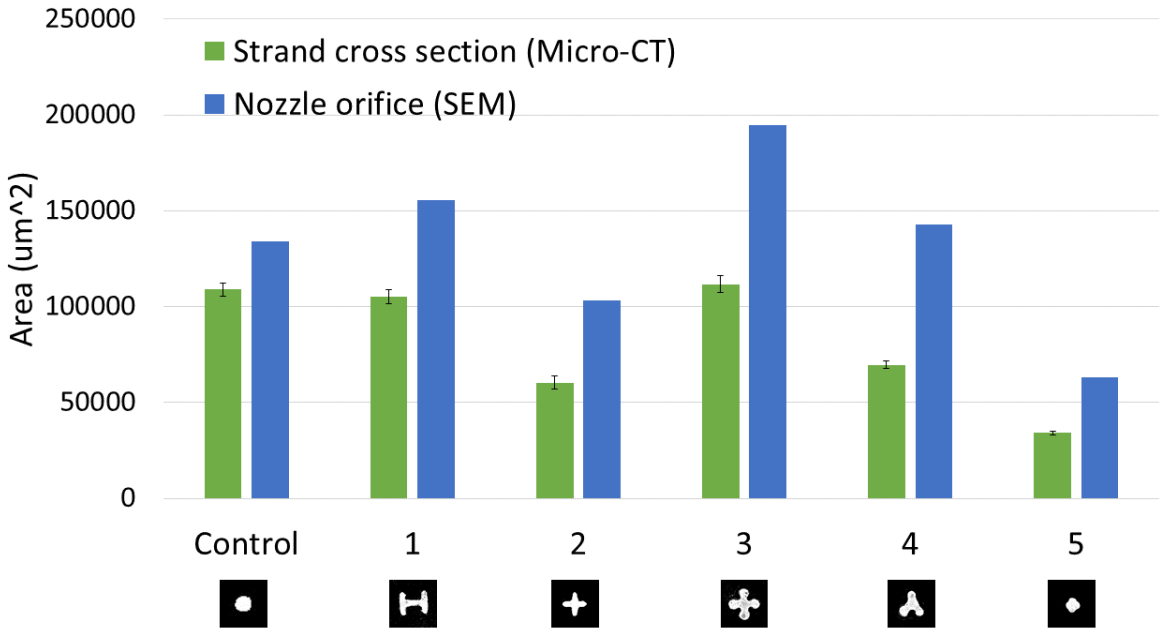

Figure 15. Area values.

It can be see that there are very big differences between the values of Micro-CT and SEM, and that the SEM values are quite bigger than the Micro-CT. This can be because we are comparing two different things (Strand cross section and Nozzle orifice). Another possible reason that the difference is so large may be due to the resolution of the images, like it can be seen in the Figure 16.

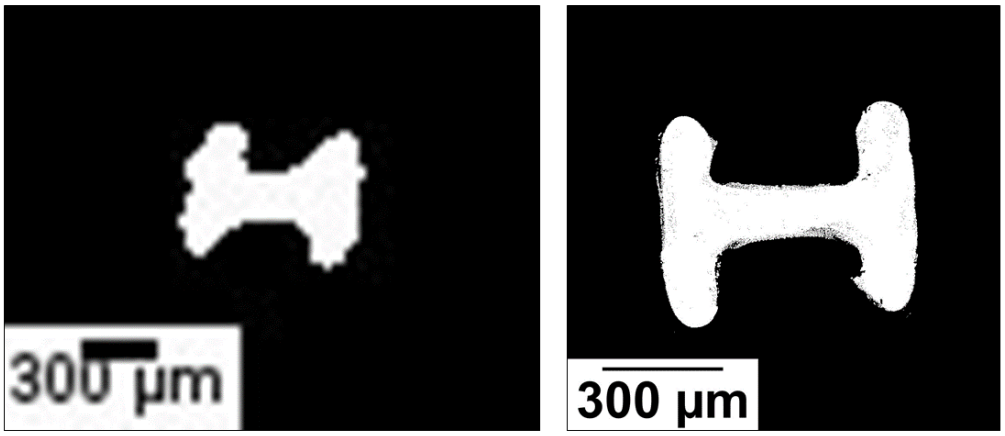

Figure 16. Comparison of the resolution of one edge of the geometry in the pattern 1 acquired in Micro-CT and SEM.

The poor resolution of the Micro-CT images affects negatively in the result; however, although it affects the result, the global trend is maintained.

Other result was the perimeter values that it can be seen in the Table 3 and the Figure 17.

Table 3. Perimeter values

	Strand cross section (Micro-CT) , um	**Nozzle orifice (SEM), um**
Control	1253± 35	1297
1	1698± 59	6236
2	1151± 38	2655
3	1584± 64	5149
4	1100± 10	2842
5	640± 35	1197

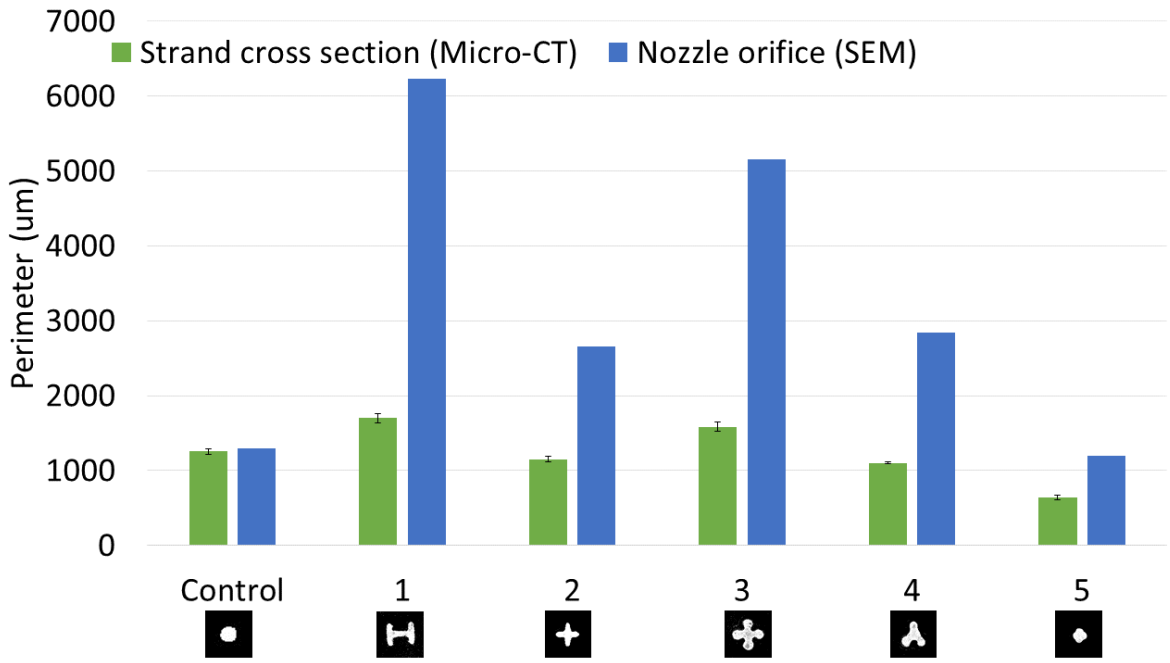

Figure 17. Perimeter values

The results have the same trend as the area results; however, the differences are bigger than the other results. The pattern control and the pattern 5 have the most similar parameters; this it is because the resolution. Like it is explaining in the area results, the Micro-CT strand images have a very poor resolution, so the complex shapes like pattern 1 or pattern 3 present have very big differences between Micro-CT and SEM images. However, the simple pattern like control and pattern 5 present less difference because simple forms do not lose so much information in low resolutions. Another important information that can be extracted is that despite everything, the global trend is still preserved.

The differences are more pronounced in this method than the area method, and this will condition the measures derived from these calculous like specific surface area and porosity.

3.3. Porosity Percentage of the scaffolds

The porosity percentage results are summarised in the Table 4 and represented in the Figure 18.

Table 4. Porosity Percentage.

	ImageJ (%)	CTAn (%)	MeshMixer (%)	Theoretical approximation (%)
Control	46.11	45.92	45.46	49.70± 1.53
1	36.68	36.32	35.85	38.78±2.14
2	47.01	46.54	46.47	50.80± 2.83
3	47.86	46.65	46.99	45.85± 2.02
4	52.26	52.04	52.47	51.88± 1.38
5	56.02	55.66	55.99	56.05± 1.22

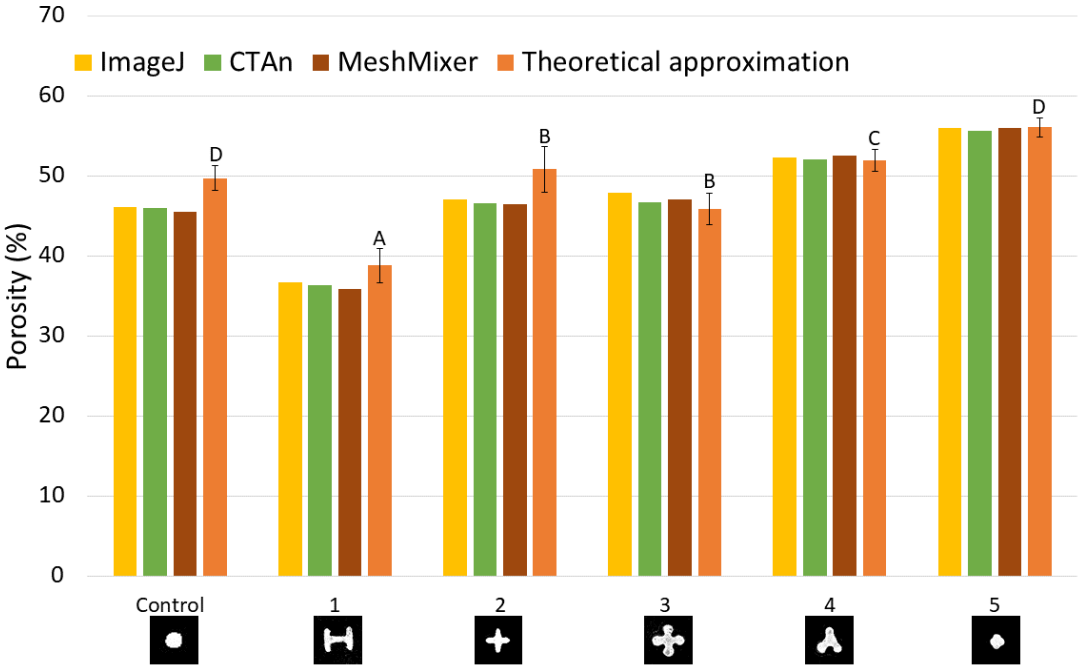

Figure 18. Porosity Percentage. Statistically significant differences indicated with different letters (p=0.05)

These results validate the four porosity measurement techniques as the results found in the four cases follow a similar trend. However, we observe that the results obtained with methods (Image J and CTAn) that derive from the same analysis technique (micro CT) present very similar values while the manually measured porosity percentage presents considerably higher deviations of no more than a 5%. Also, the MeshMixer analysis presents similarity with the other methods.

We can affirm that most porous scaffold is the pattern 5 and the less porous one the pattern 1. We also observe how the porosity of patterns 2 and 3 are slightly different while having a very similar shape and this can be explained by the fact that, as we have fixed the pore size in the printing settings (250 µm), the equivalent diameter is the parameter that determines the porosity. Figure 19 illustrates this situation: All the scaffolds have the same gap between strands, so if the strand have less area and then less equivalent diameter, we will have more porosity in the structure.

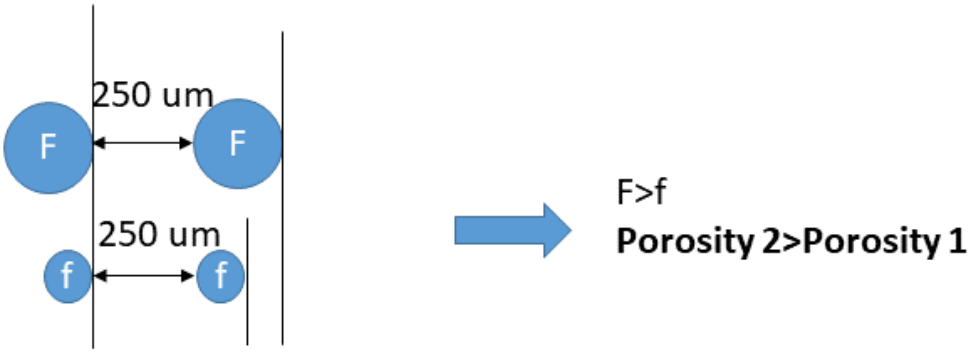

Figure 19. Schema representing the influence of strand's area on the porosity percentage of the scaffold.

Another results about porosity percentage is the percentage of open and closed porosity, this value can be seen in the Table 5 and more graphically in the Figure 20. Notice that these measurements could only be made with CTAn as it is the only software presenting this feature.

Table 5. Open and closed porosity values measured with CTAn.

	Closed porosity (%)	**Open porosity (%)**
Control	0.001	45.916
1	0.067	36.278
2	0.198	46.521
3	0.004	46.652
4	0.001	52.038
5	0.001	55.655

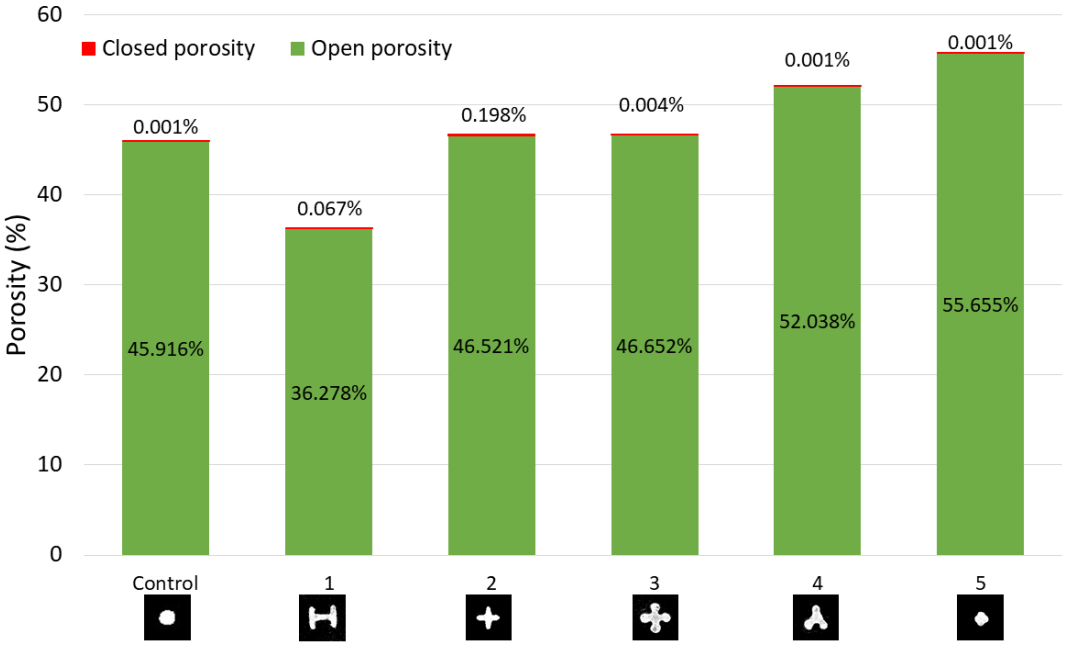

Figure 20. Open and Closed porosity.

It can be seen that the majority of the porosity is open porosity and this its logical because the printing method used (robocasting) and the settings chosen where intendedly seeking to obtain an interconnected pore network to allow the tissue colonisation of the scaffold. The closed pores observed are either microscopic air bubbles entrapped inside de ink or noise of the Micro-CT interpreted as pores. In any case, these values are neglectable compared to the open porosity values.

3.4. Pore size distribution of the scaffolds

This results of the pores size distribution measured with CTAn can be observed in Table 6 and Figure 21.

Table 6. Pore size distribution values.

	Control	**1**	**2**	**3**	**4**	**5**
26 - <79	1.02	2.16	1.27	0.84	0.82	0.87
79 - <132	3.43	6.64	2.37	3.70	2.91	3.65
132 - <185	4.31	7.66	3.40	5.04	3.44	4.74
185 - <238	14.78	12.86	7.68	8.21	7.32	10.17
238 - <291	24.35	14.41	12.62	10.10	9.97	17.22
291 - <344	27.75	13.76	21.08	10.46	11.48	18.61
344 - <397	22.54	17.99	35.66	21.81	17.23	23.71
397 - <450	1.81	13.62	12.99	18.67	17.09	14.11
450 - <503	0	6.98	2.79	11.35	13.25	4.97
503 - <556	0	3.72	0.14	5.90	8.92	1.77
556 - <609	0	0.19	0	3.06	3.58	0.17
609 - <662	0	0	0	0.85	2.41	0
662 - <715	0	0	0	0	0.83	0
715 - <768	0	0	0	0	0.74	0

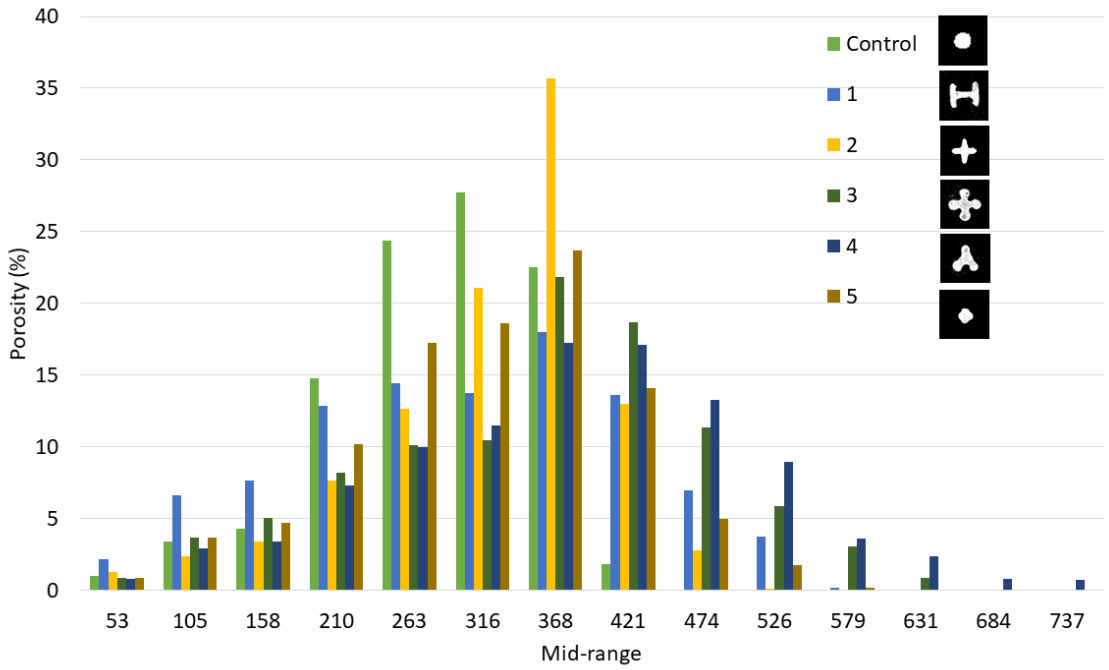

Figure 21. Pore size distribution.

Like it can be seen in the Figure 21, the mid-range pore size ranges between 300 µm and 400 µm. The pattern 2 has the sharpest and biggest peak which indicates a very homogeneous porosity. On the other hand, pattern 4, presents the widest distribution and this could be attributed to its low

reproducibility that led to varying pore sizes depending on the strand irregular deposition. (see Figure 14 to compare the regularity of the different structures with the distribution scaffold main peak sharpness).

3.5. Specific surface area of the scaffolds

The SSA values are reported in Table 7 and Figure 22.

Table 7. Specific Surface values

	ImageJ, um^3/um^2	CTAn, um^3/um^2	MeshMixer, um^3/um^2	Theoretical approximation, um^3/um^2
Control	0.011	0.011	0.02	0.011
1	0.030	0.027	0.02	0.033
2	0.039	0.035	0.03	0.038
3	0.033	0.030	0.02	0.031
4	0.036	0.032	0.02	0.034
5	0.046	0.042	0.03	0.040

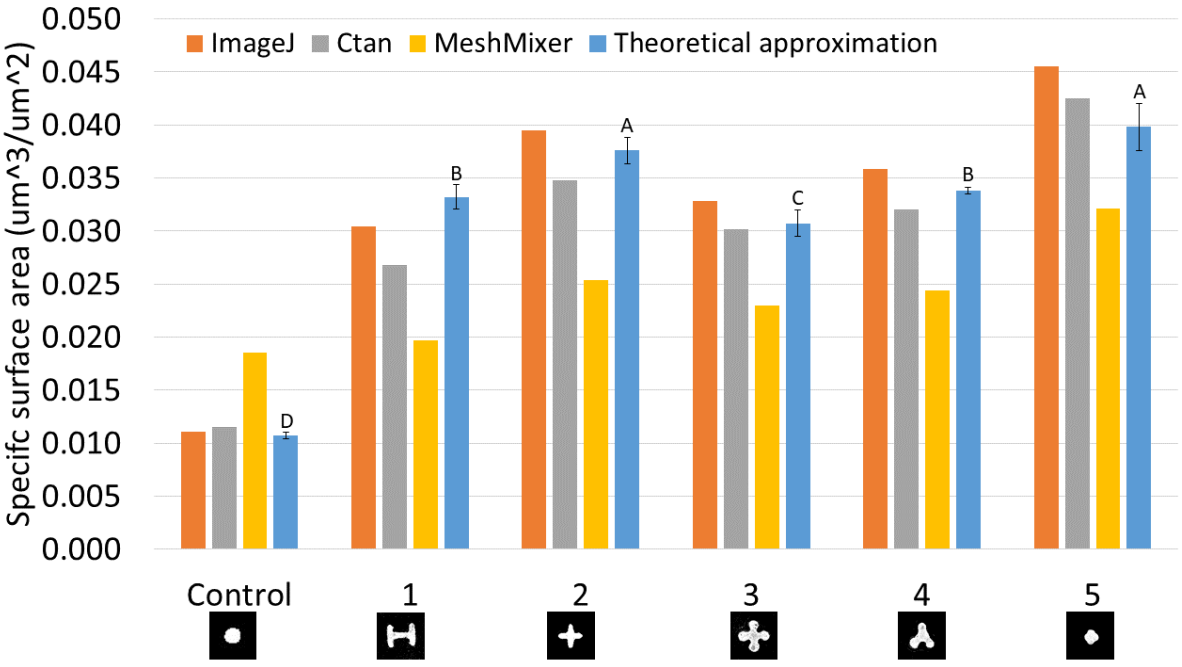

Figure 22. Specific Surface Values. For the theoretical approximation, letters above the error bar represent statistically significant differences (p=0.05)

In this case, there are bigger differences between CTAn and ImageJ than the ones observed for the measures of porosity percentage. This difference can be due how the programs calculates these

parameters. Like it is explain before (see 2.3.4.1), the CTAn and the ImageJ calculate these values in a different way; the CTAn calculates this values by using a skeletonisation and a sphere fitting while ImageJ calculate this value by estimating the fractal dimension on topographic surfaces [29]. The MeshMixer values have a lot of difference with respect to the other methods, this may be due because in the mesh stage, resolution is lost and that is transformed into the differences observed.

"Control" is the pattern that presents a lowest specific surface area. This is because the circle is the figure that has the highest area in the least perimeter possible. On the other hand, the geometry with a highest SSA is 2. This phenomenon is not only explained only for its more imbricated structure than the circular profile, because there are other imbricated cross sections, but also due to its small size. A small section will require a higher number of filaments to print a same volume leading to a higher surface area in the final structure. Figure 23 illustrates both scenarios.

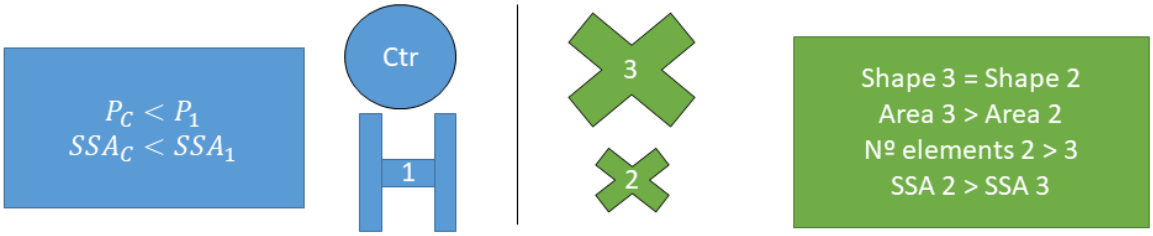

Figure 23. Schema depicting the differences in SSA as a function of different cross section parameters.

3.6. Concavity of the nozzle and strands

The three methods used to quantify the concavity do not correspond to the same unities and they are only comparable in terms of trends. For this reason, this section will be divided in the different approaches used:

3.6.1. Surface indexes of the nozzle and strand sections

There is no data on the concavity of the pattern control in the SEM images because it did not have its disk to do the SEM analysis. These parameters were evaluated for the strand cross section and the nozzle orifices with two methods:

A) Perimeter concavity ratio

The values of the perimeter concavity ratio can be found in the Table 8 and are represented in a bar chard in the Figure 24. It should be pointed out that some values could only be calculated with the SEM images as the scaffolds could not be successfully printed and therefore there is no Micro-CT data.

Table 8. Perimeter concavity ratios of the different sample conditions

	Strand cross section (Micro-CT), arb Unit	**Nozzle orifice (SEM), arb Unit**
Control	1.02±0.03	N/A
1	1.14±0.04	3.02
2	1.08±0.04	1.79
3	1.11±0.05	2.60
4	1.01±0.01	1.67
5	1.00±0.06	1.28

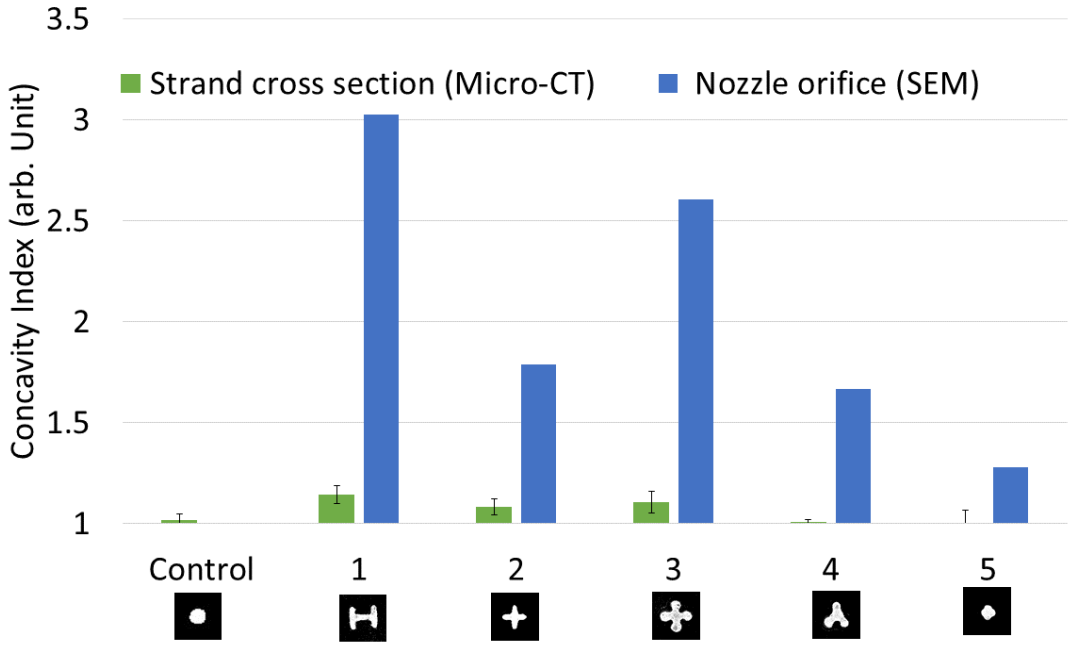

Figure 24. Concavity Index by Perimeter. No statistically significant differences were found in the condition Micro-CT (p=0.05).

We observe a big difference between the measurements carried out on the nozzle and the scaffold cross-section. This could illustrate the deviation between them but also could be attributed to the big differences or resolution of the two techniques used (see Figure 16).

Ideally what should be done to have trustfully data of the strands with high resolution is preparing cross sections of the scaffolds and analysing them by scanning electron microscopy.

The fact that we do not observe statistically significances in the different concave strands when we do an ANOVA test indicates that this index presents a low sensitivity towards the concavity degree in the structure. For this reason, it may not be the most suitable to compare the degree of concavity in the geometries.

B) Surface concavity percentage

Surface concavity percentages for the different samples conditions are reported in Table 9 and in the Figure 25.

Table 9. Surface concavity percentage values.

	Strand cross section (Micro-CT), %	**Nozzle orifice (SEM), %**
Control	7.69±3.92	N/A
1	31.06±4.18	47.11
2	20.51±5.63	31.29
3	21.77±4.93	31.13
4	12.96±2.72	25.69
5	7.08±4.47	5.15

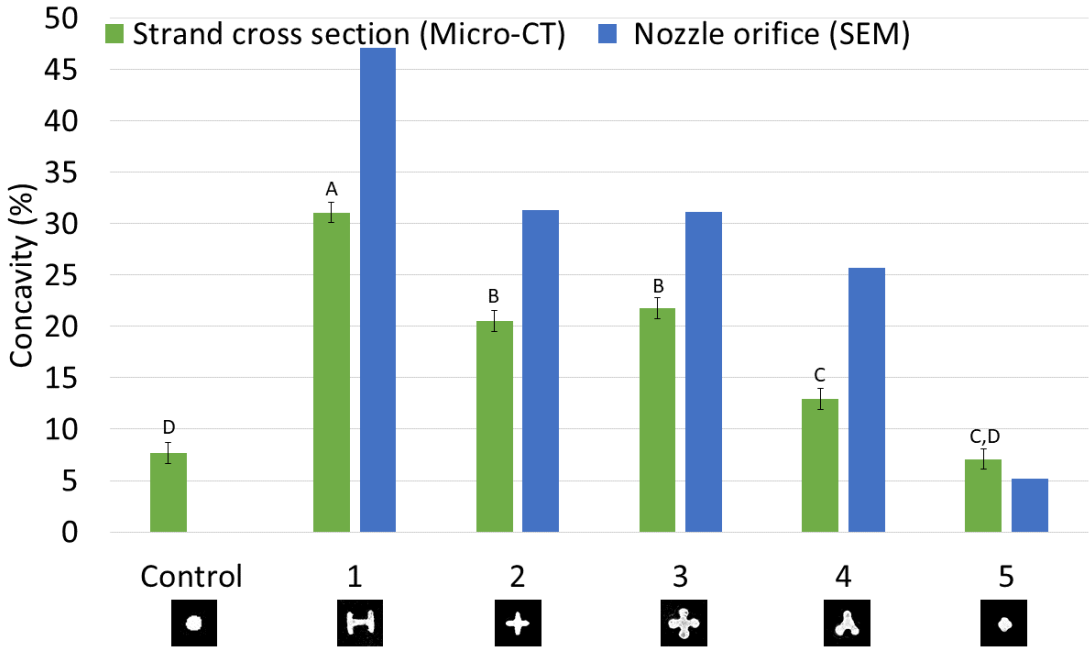

Figure 25. Surface concavity percentage values. For the "Micro-CT" condition, letters above the error bar represent statistically significant differences (p=0.05)

This method resulted to present a higher sensitivity towards concavity that the perimeter concavity ratio. This higher sensitivity allows us to observe trends in the different patterns with pattern 1 exhibiting the highest concavity and the control and pattern 5 presenting the lowest concavity. This results are coherent with the intuitive judgements that we can make of these geometries.

With this index, we observe a higher similarity between results of measurements in SEM and Micro-CT images. Provably this is due to the fact that the perimeter measurements are more sensitive to the resolution of the image than the area measurements.

3.6.2. Volumetric convexity assessment of the scaffolds

Table 10 summarizes the results of convexity obtained with the Quickhull Algorithm [30]. The values are represented a bar chart in Figure 26.

Table 10.Convexity measurements by "Quickhull" algorithm

	Quickhull 3D convexity Index (arb. Unit)
Control	0.37
1	0.19
2	0.18
3	0.21
4	0.22
5	0.31

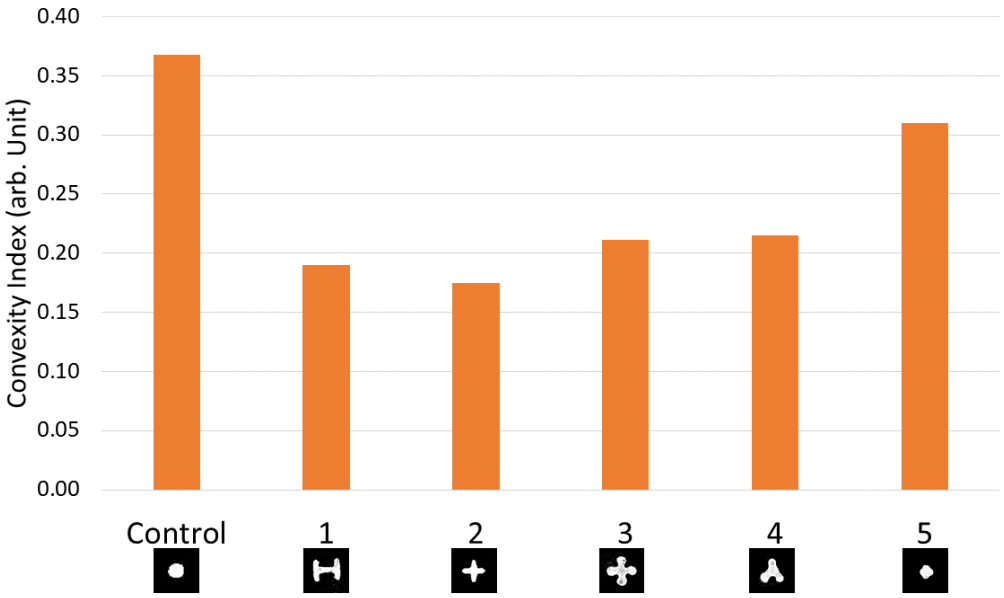

Figure 26. Convexity measurements by "Quickhull" algorithm.

These values show that the control is the most convex pattern whilst the other patterns have a very similar convexity. This first observation is consistent with the fact that the cylinder is the most convex of the shapes analysed. On the other hand, this method presents a low sensitivity among different concave structures; this it is because the 3D scaffold is composed by cylinders, so their convexity will be very similar between then.

Conclusions

After all this project, three different techniques were validated and compared in order to calculate 3D and 2D image parameters. Also, new strategies to define attributes such as concavity and specific surface area were defined.

In the results, different significant parameters were observed like specific surface area and concavity between the samples and, finally, it has been see that the best way to measure concavity in 2D it is by percentage of area, because it has more sensitivity than the method by perimeter.

After all this project, for the 3D parameters (porosity and concavity), four techniques have been tested and validated: CTAn, ImageJ, MeshMixer and manually. These techniques were validated by comparing and evaluating their differences. In the other hand, for the 2D parameters it was found a method in the literature to measure concavity; however, in this work two more method were developed: By using the cross section perimeter and area. In the results it can be seen that the area method has a greater sensitivity than the perimeter method; so, the area method is the most appropriate to calculate the concavity.

From the geometrical parameters like area and perimeter we see that there are big differences between the disc images (SEM) and the strand images (Micro-CT); these differences are because it is being compared the images of the nozzle orifice (obtained by SEM) with the experimental values (strand images). These differences attributed to the accentuated differences of resolution that both acquisition/ imaging methods present. However, despite of the differences between the values, they have the same tendency.

In the porosity results there were no large differences between the scaffolds. This it is because the scaffolds were printed in a pre-setting conditions so that they would give an equivalent porosity and be able to compare the samples between them (250 μm). A good indicator about that was the pore size distribution results. The peaks in the graph represent regularity and good print quality.

In the specific surface area, the pattern which has the highest coefficient was the 5 and the lowest the Control. These results are coherent because the control section is a circle, so it has the least surface/area coefficient and the pattern 5; despite of being small, it was repeated very frequently, causing the sum of all the filaments to give a larger surface than the other patterns. Also, the MeshMixer method have the too much error compared to the other methods, this can be due how the plugin 3D Viewer do the meshing process from the Micro-CT scaffolds before the MeshMixer calculous, however, more trials are necessary to ensure this hypothesis.

In the concavity results, the pattern with higher concavity percentage by the area method was the pattern 1. This is because it is the section with higher complexity and this produces a greater concavity of the section. Also, we see that the resolutions affect negatively to the 2D calculous as the geometrical parameters. Another important thing is that calculate the concavity by area have a higher sensitivity and credibility that the perimeter method (this was observed by the ANOVA analysis); so it is more advisable to calculate the concavity of the strand by area than by perimeter.

For the convexity analysis, the values between the scaffold were pretty similar, because the concavity of the filament strand is not large enough compared to the length of the cylinder to produce significant differences between the scaffolds. However, there was a difference between the pattern control and the pattern 5 of the rest; this is because pattern 5 has a strand section very similar to that of a circle, so it is very similar to pattern control.

Finally, to sum up, we have seen how each program calculates similar parameters with different approaches, although it may affect the result to a greater or lesser extent, and the results can be compared without problems. Ways to calculate porosity, specific surface area and concavity in two dimensions have been validated, extrapolating it to three dimensions, as a viable alternative to direct 3D calculation. Although Micro-CT is a very promising and interesting technique, resolution limitations may appear compared to more traditional techniques such as SEM. And, finally, that more and more these techniques are used in papers in order to calculate some parameters that, in other ways, will be time-consuming and expensive. This work can help those people to see a review of some image processing methods, how to use their and their liability.

If we want to choose a scaffold from all those we have analysed, we will choose the pattern that has the best porosity, specific surface, reliability and concavity. First, we need to discards the pattern 1 and 3 to focus in the patterns 2, 4 and 5. The pattern 1 has a small difference in area with its SEM image and the highest convex index; however, it has the highest difference in the perimeter with its SEM image and the lowest porosity of all scaffolds. In the other hand, the pattern 3 have a high difference in the perimeter with its SEM image and one of the lowest specific surface area.

For the pattern 2, has a small difference in the area and perimeter with its SEM image, a very high porosity with the best homogenous pixel size (this means that it has the highest quality printing process of all scaffolds), a very high specific surface area; however, it has the highest closed porosity of all scaffolds (0.198 %). The pattern 4 has a small difference in the area with its SEM image and high porosity; however, it has a high difference in the perimeter with its SEM image and a low concavity percentage. Finally, the pattern 5 have the smallest difference in the area and perimeter with its SEM image and the highest porosity and specific surface of all scaffold; however, it has the lowest concavity percentage. So, finally, the scaffold chose is the pattern 2, because it has no serious characteristics where it fails (its closed porosity percentage is less than 0.5 %).

Future perspectives

After doing these review to some image processing methods, the SEM analysis was only possible to do with the disc; so, the strand section of the scaffold can be put in resin in order to make SEM image processing and compare them to the SEM disc images.

Economic analysis

The programs used in this project where CTAn, CTVox, Data Viewer, ImageJ (Fiji), MeshMixer and Minitab.

The programs CTAn, CTVox and Data Viewer where from the same company, Bruker. These programs were included in the Micro-CT, so there is a need of rent a Micro-CT from other lab or company.

ImageJ and MeshMixer are free code programs so, the programs and the plugin are free to use.

Minitab on the other hand, is a payment program, however, if a UPC student use it, it will receive a free copy during the academic stay. However, if this is not the case, the licence cost for one user can cost up to 1996.50 euros (see Table 11).

Also, we have to take into account the human resources analysis in Table 12.

The total cost of this analysis techniques it is seen in the Table 13.

Table 11. Economic analysis.

TECHNIQUE	UNIT PRICE (€/H)	TIME PER SAMPLE	N^{O} SAMPLES	COST
MICRO -CT	18	1.16h	6	125.28€
IMAGEJ	FREE (0€)	-	-	0€
SEM	9	0.3h	5	13.5€
MESHMIXER	FREE (0€)	-	-	0€
MINITAB	FREE (UPC licence)	-	-	0€
TOTAL				**138.78€**

Human resources

Table 12 Human resources analysis

POSITION	UNIT PRICE (€/H)	QUANTITY (H)	COST
Project director	60	45 h	2700 €
PhD student	30	80 h	2400 €
Undergraduate student	-	600 h	0€
TOTAL			**5100 €**

Table 13. Total cost

FINAL PRICE	COST
ANALYSIS TECHNIQES	138.78€
HUMAN RESOURCES	5100 €
TOTAL	**5238.78 €**

References

[1] A. Barba *et al.*, "Osteogenesis by foamed and 3D-printed nanostructured calcium phosphate scaffolds: Effect of pore architecture," *Acta Biomater.*, vol. 79, pp. 135–147, 2018.

[2] G. Hannink and J. J. C. Arts, "Bioresorbability, porosity and mechanical strength of bone substitutes: What is optimal for bone regeneration?," *Injury*, vol. 42, no. SUPPL. 2, Sep. 2011.

[3] C. M. Bidan *et al.*, "How linear tension converts to curvature: Geometric control of bone tissue growth," *PLoS One*, vol. 7, no. 5, May 2012.

[4] A. Barba *et al.*, "Osteoinduction by Foamed and 3D-Printed Calcium Phosphate Scaffolds: Effect of Nanostructure and Pore Architecture," *ACS Appl. Mater. Interfaces*, vol. 9, no. 48, pp. 41722–41736, 2017.

[5] H. Chen, C. Wang, X. Zhu, K. Zhang, Y. Fan, and X. Zhang, "Fabrication of porous titanium scaffolds by stack sintering of microporous titanium spheres produced with centrifugal granulation technology," *Mater. Sci. Eng. C*, vol. 43, pp. 182–188, Oct. 2014.

[6] A. Mikos and J. Temenoff, "Formation of highly porous biodegradable scaffolds for tissue engineering," *Electron. J. Biotechnol.*, vol. 3, no. 2, pp. 23–24, 2000.

[7] C.-J. Liao, C.-F. Chen, J.-H. Chen, S.-F. Chiang, Y.-J. Lin, and K.-Y. Chang, "Fabrication of porous biodegradable polymer scaffolds using a solvent merging/particulate leaching method," *J. Biomed. Mater. Res.*, vol. 59, no. 4, pp. 676–681, Mar. 2002.

[8] S. Lewin, A. Barba, C. Persson, J. Franch, M. P. Ginebra, and C. Öhman-Mägi, "Evaluation of bone formation in calcium phosphate scaffolds with μcT-method validation using SEM," *Biomed. Mater.*, vol. 12, no. 6, pp. 1–21, 2017.

[9] R. B. Rao, K. L. Krafcik, A. M. Morales, and J. A. Lewis, "Microfabricated deposition nozzles for direct-write assembly of three-dimensional periodic structures," *Adv. Mater.*, vol. 17, no. 3, pp. 289–293, 2005.

[10] M. F. M. Costa, "APPLICATION OF IMAGE PROCESSING TO THE CHARACTERISATION OF NANOSTRUCTURES *," 2004.

[11] L. Zeman and L. Denault, "Characterization of microfiltration membranes by image analysis of electron micrographs. Part I. Method development," *J. Memb. Sci.*, vol. 71, no. 3, pp. 221–231, Jul. 1992.

[12] F. A. AlMarzooqi, M. R. Bilad, B. Mansoor, and H. A. Arafat, "A comparative study of image analysis and porometry techniques for characterization of porous membranes," *J. Mater. Sci.*, vol. 51, no. 4, pp. 2017–2032, 2016.

[13] V. Guarino, L. Ambrosio, A. Guaccio, and P. A. Netti, "Image processing and fractal box counting: User-assisted method for multi-scale porous scaffold characterization," *J. Mater. Sci. Mater. Med.*, vol. 21, no. 12, pp. 3109–3118, 2010.

[14] C. Grove and D. A. Jerram, "JPOR: An ImageJ macro to quantify total optical porosity from blue-stained thin sections," *Comput. Geosci.*, vol. 37, no. 11, pp. 1850–1859, 2011.

[15] M. L. Mather *et al.*, "Image-based characterization of foamed polymeric tissue scaffolds," *Biomed. Mater.*, vol. 3, no. 1, Mar. 2008.

[16] E. T. G. De Souza, M. D. Nunes Tameirão, J. M. Roter, J. T. De Assis, A. De Almeida Neves, and G. A. De-Deus, "Tridimensional quantitative porosity characterization of three set calcium silicate-based repair cements for endodontic use," *Microsc. Res. Tech.*, vol. 76, no. 10, pp. 1093–1098, 2013.

[17] S. M. Plaza, L. K. Scheffer, and M. Saunders, "Minimizing Manual Image Segmentation Turn-Around Time for Neuronal Reconstruction by Embracing Uncertainty," *PLoS One*, vol. 7, no. 9, Sep. 2012.

[18] Z. Püspöki, M. Storath, D. Sage, and M. Unser, *We give a methodology-oriented perspective on directional image analysis and rotation-invariant processing. We review the state of the art in the field and make connections with recent mathematical developments in functional analysis and wavelet theory. W*. 2016.

[19] J. Schindelin *et al.*, "Fiji: An open-source platform for biological-image analysis," *Nature Methods*, vol. 9, no. 7. pp. 676–682, Jul-2012.

[20] N. Jamil, T. M. T. Sembok, and Z. A. Bakar, "Noise removal and enhancement of binary images using morphological operations," in *Proceedings - International Symposium on Information Technology 2008, ITSim*, 2008, vol. 3.

[21] "Sensors and Platforms."

[22] K. Hassan, J. C. Dort, G. R. Sutherland, and S. Chan, "Evaluation of software tools for segmentation of temporal bone anatomy," in *Studies in Health Technology and Informatics*, 2016, vol. 220, pp. 130–133.

[23] B. Schmid, J. Schindelin, A. Cardona, M. Longair, and M. Heisenberg, "A high-level 3D visualization API for Java and ImageJ," *BMC Bioinformatics*, vol. 11, May 2010.

[24] M. Doube *et al.*, "BoneJ: Free and extensible bone image analysis in ImageJ," *Bone*, vol. 47, no. 6, pp. 1076–1079, Dec. 2010.

[25] C. Bruker-Mikro-CT, "The user ' s guide - ALLE," *Hand*, pp. 1–112, 2010.

[26] Bruker-MicroCT team, "Introduction to porosity analysis Method note," *Method note*, no. June, pp. 1–17, 2014.

[27] "Morphology - Skeletonization/Medial Axis Transform." [Online]. Available: https://homepages.inf.ed.ac.uk/rbf/HIPR2/skeleton.htm. [Accessed: 22-Dec-2019].

[28] J. C. Castilla-Rho, G. Mariethoz, B. F. J. Kelly, and M. S. Andersen, "Stochastic reconstruction of paleovalley bedrock morphology from sparse datasets," *Environ. Model. Softw.*, vol. 53, pp. 35–52, 2014.

[29] K. G. Sheets *et al.*, "Microglial ramification and redistribution concomitant with the attenuation of choroidal neovascularization by neuroprotectin D1.," *Mol. Vis.*, vol. 19, pp. 1747–59, 2013.

[30] Dirk Gregorius, "Implementing Quickhull," 2014.

[31] Minitab, "Introducción a Minitab 19 para Windows," 2019.